Solar-Terrestrial Physics, 2018. Vol. 4. Iss. 1, pp. 12–24, DOI: 10.12737/stp-41201802. © 2018 B.B. Krissinel Published by INFRA-M Academic Publishing House
Original Russian version: B.B. Krissinel, published in Solnechno-zemnaya fizika, 2018, vol. 4, iss. 1, pp. 14–27, DOI: 10.12737/szf-41201802 © 2018 INFRA-M Academic Publishing House (Nauchno-Izdatelskij Centr INFRA-M)

INTENSITY OF EMISSION LINES OF THE QUIESCENT SOLAR CORONA: COMPARISON BETWEEN CALCULATED AND OBSERVED VALUES

B.B. Krissinel
Institute of Solar-Terrestrial Physics SB RAS,
Irkutsk, Russia, krissinel@iszf.irk.ru

Abstract. The paper reports the results of calculations of the center-to-limb intensity of optically thin line emission in EUV and FUV wavelength ranges. The calculations employ a multicomponent model for the quiescent solar corona.

The model includes a collection of loops of various sizes, spicules, and free (inter-loop) matter. Theoretical intensity values are found from probabilities of encountering parts of loops in the line of sight with respect to the probability of absence of other coronal components. The model uses 12 loops with sizes from 3 200 to 210 000 km with different values of filling factor and pressure at the loop base and apex. The temperature at loop apices is 1 400 000 K. The calculations utilize the CHIANTI database. The comparison between theoretical and observed emission intensity values for coronal and transition region lines obtained by the SUMER, CDS, and EIS telescopes shows quite satisfactory agreement between them, particularly for the center of the solar disk. For the data acquired above the limb, the enhanced discrepancies after the analysis refer to errors in EIS measurements.

Keywords: Sun—corona, UV radiation, atomic data.

INTRODUCTION

Measurements of coronal plasma characteristics are important for understanding various processes occurring in the solar atmosphere, such as coronal heating and coronal mass ejections, as well as structure and physical characteristics of active regions, prominences, and coronal holes. The solar corona in the ultraviolet wavelength range has been studied for a long time. Nowadays, a number of excellent satellite-borne spectrographs allow detailed diagnostics of the electron density and temperature of solar plasma. The diagnostics based on observed intensities of optically thin lines [Mason, Monsignori Fossi, 1994; Laming et al., 1997] employs calculations of emission from transitions of excited ionic levels. Established in 1997 and continuously updated atomic database CHIANTI [Dere et al., 1997; Landi et al., 2012] also contains a software package for such calculations.

By now, a fairly large number of studies have been published on plasma of solar quiescent and active regions. The analysis of UV emission lines provides insight into plasma characteristics, but at the same time it allows us to identify problems arising from inaccurate atomic data and errors in spectroheliogram processing. Atomic data are obtained largely via calculations, and the accuracy of calculations can be verified against a stable emission source – the emission from quiescent regions of the solar atmosphere. The quiescent corona above the limb at distances 1.03–1.3 solar radius has been studied in [Feldman et al., 1998, 1999; Warren, 1999; Allen et al., 2000; Landi et al., 2002a, 2002b; Warren, Warshall, 2002; Feldman, 2009; Mohan et al., 2003; Parenti et al., 2003; Warren, Brooks, 2009], in which the coronal plasma at such heights is assumed to be isothermal.

In [Warren, 2005; Brooks, Warren, 2006; Brooks et al., 2009], the plasma observed at the solar disk center is examined. The temperature of the emitting layer was taken here to be equal to the temperature of ionization maximum of a given ion. Validity of such approximations can be assessed by calculating the emission line intensity with a quiescent solar corona model.

This paper employs a multicomponent model of the quiescent solar corona [Krissinel, 2015], which allows us to obtain equatorial center-to-limb distributions at wavelengths from 1 to 100 cm. These distributions agree well with experimental ones. In this model, the distribution of components over the solar disk is a random process with constant variance and averages. In this case, solar emission can be represented by the emission of a discrete set of corona components.

The purpose of this paper is to compare emission intensity calculations made with a solar corona model developed from radio observations to the reported observations of EUV and FUV emission lines obtained with the SOHO/CDS, SOHO/SUMER, and HINODE/EIS spectrographs. When adapting the model to calculations of the equatorial distribution of the coronal line intensity, special attention is paid to the choice of the type of fractional ionization and to height density and temperature profiles in the transition region of loops.

1. FUNDAMENTALS

To calculate the emission line intensity in quiescent coronal regions, a technique is used which was proposed by Krissinel [2015] for centimeter and decimeter wavelengths.

According to this technique, the entire set of coronal loops is represented as a set of loops ranked by their

size, with plasma parameters average for loops of a given size range. Similarly, the presence of spicules – rapidly changing structures in the solar chromosphere – is taken into account. Given height profiles of temperature and electron density of loops and spicules as well as parameters of free (inter-loop) matter, we can find the total coronal emission intensity by integrating emission from parts of loops and spicules, and also from free matter along the line of sight. The contribution of emission from each part of loop, spicule or free matter is determined by plasma parameters of this part as well as by the probability of appearance of these parts along the line of sight.

Determination of height profiles of temperature and density of loops and free matter is closely related to a quiet atmosphere model for the solar disk center, hereinafter referred to as "initial" and obtained by combining the coronal part (starting at h_0=2275 km) of the model, described in [Getman, Livshits, 1996], and combinations of FALA and FALF models of the chromosphere and transition region [Fontenla et al., 1993] in the relation FALA·0.965+FALF·0.035.

The loop structure is represented as a set of 10 loops with sizes proportional to the mean size of the chromospheric network, i.e. with radii $R_{\rm loop}$ from 15 000 to 210 000 km, and also with significantly smaller sizes: $R_{\rm loop}$=7 200, 3 100 km. The loop thickness is also assumed to be constant over the entire length and is $R_{\rm loop}/15$. By comparing calculated and experimental data, Krissinel [2015] has found the main parameters of the loop structure: $T_{\rm maxloop}$ is the temperature of loop apices, p_0 is the pressure at h_0, p_1 is the pressure at the loop apex, the filling factors α_r (the number of loops of a given size located in a $2R_{\rm loop}\times 2R_{\rm loop}$ area).

The h dependence of the coronal part of loop is given by

$$T_{\rm lp}(h)=T_{\rm min}+(T_{\rm maxloop}-T_{\rm min})\times \\ \times(\sin(\pi/2\cdot(h-h_0)/(R_{\rm loop}-h_0)))^{a_{\rm lp}}, \quad (1)$$

where $a_{\rm lp}$ is the parameter determining the degree of profile squareness, $T_{\rm min}$ is the temperature in the initial model at h_0. Below h_0, the loop temperature profiles correspond to the initial model.

The electron density of the coronal part of loop is found from

$$n_{\rm elp}(h)=p_0\exp(-(h-h_0)/\lambda_{\rm p0})/(2k_{\rm Bolz}T_{\rm lp}(h)), \quad (2)$$

where $k_{\rm Bolz}$ is the Boltzmann constant, $\lambda_{\rm p0}=(R_{\rm loop})/\ln(p_0/p_1)$. In the region of loop feet, the electron density is determined from the initial model profile $n_{\rm e}(h)$:

$$n_{\rm elp}(h)=n_{\rm e}(h)p_0/p_{\rm sh}, \quad (3)$$

where $p_{\rm sh}$ is the pressure in the initial model at h_0.

For spicules, stratification (the relative area of the solar disk covered with spicules reaching a certain height) proposed in [Lantos, Kundu, 1972] is taken as a basis, supplemented with a more detailed ranking of spicules in size and probability of location at certain heights.

To calculate probabilistic characteristics of parts of loops along the line of sight, all loops are divided in height into separate segments, the upper of which is the loop apex. Then, the probability of encountering a line of sight in these segments $P_{\rm vk}$ is computed from their projections on the horizontal plane. This allows us to find $\Delta h_{\rm gr}$ corresponding to vertical projections of the mean free path in these segments, and probability $P_{\rm vl}$ of encountering a line of sight in such a loop layer. The probabilities $P_{\rm vsp}$ for spicules can be found in a similar way.

The obtained sequences $\Delta h_{\rm gr}$ for loops and spicules form a height grid $h_{\rm usd}$, which then is used for calculating emission intensity. When calculating the resulting intensity along the line of sight, we should account for the probability of absence of other atmospheric details $B_{\rm ls}$ in a loop segment under study. These values are determined for each interval $\Delta h_{\rm gr}$ and represent the product of probabilities of absence of other loops and spicules in this interval. For the free matter the probability of absence of loops and spicules $N_{\rm bls}$ is found at each height $h_{\rm usd}$ as a product of probabilities of absence of parts of loops and spicules in the vicinity of this height, which are equal to the nearest interval $\Delta h_{\rm gr}$ of these elements.

Hence, the emission line intensity $I(i)$ of quiescent solar regions can be derived from the formula

$$I(i)=I(i-1)+\eta(i-1)\times \\ \times\left(\sum_{j=0}^{n} I_{\rm lp}(i,\,j)P_{\rm vl}(l,\,j)B_{\rm ls}(l,\,j)\right)+I_{\rm sv}(i)N_{\rm bls}(i), \quad (4)$$

where

$$\eta(i)=\eta(i-1)\left(\sum_{j1=0}^{n1} P_{\rm vl}(l,\,j_1)B_{\rm ls}(l,\,j_1)+N_{\rm bls}(i)\right), \quad (5)$$

Here $I_{\rm lp}(i, j)$ is the emission intensity of the jth loop between $h_{\rm usd}(i-1)$ and $h_{\rm usd}(i)$; $I_{\rm sv}(i)$ is the emission intensity of free matter in the same height interval. The emission intensity of each jth loop is calculated from its own height grid $\Delta h_{\rm gr}(l, j)$, therefore, when calculating by (4), the j_1 loop emission whose lower boundary $\Delta h_{\rm gr}$ coincides with $h_{\rm usd}(i)$ is taken into account at each height $h_{\rm usd}(i)$.

As is known [Mason, Monsignori Fossi, 1994; Dere et al., 1997], the emissivity (power per unit volume, erg cm^{-3}s^{-1}) for an optically thin spectral line of wavelength $\lambda_{i,j}$ is

$$\varepsilon_{ij}=N_j\left(X^{+{\rm m}}\right)A_{ji}\frac{h_{\rm p}c}{\lambda_{ij}}, \quad (6)$$

and the intensity

$$I(\lambda_{ij})=\frac{h_{\rm p}\nu_{ij}}{4\pi}\int N_j A_{ji}\,dh\left[\text{erg cm}^{-2}\text{s}^{-1}\text{sr}^{-1}\right], \quad (7)$$

where $h_{\rm p}$ is the Planck constant; $\nu_{ij}=\dfrac{c}{\lambda_{ij}}$ is the frequency; i, j are the lower and upper levels; A_{ji} is the probability of spontaneous transition; N_j is the density of the upper level j of an emitting ion; and h is the line of sight through the emitting plasma. The level population j can be expressed as

$$N_j\left(X^{+\mathrm{m}}\right)=\frac{N_j\left(X^{+\mathrm{m}}\right)}{N\left(X^{+\mathrm{m}}\right)}\frac{N\left(X^{+\mathrm{m}}\right)}{N(X)}\frac{N(X)}{N(H)}\frac{N(H)}{N_\mathrm{e}}N_\mathrm{e}, \quad (8)$$

where $\frac{N\left(X^{+\mathrm{m}}\right)}{N(X)}$ is the ratio of the ion density $X^{+\mathrm{m}}$ to the total density of the element X; $Ab(X)=N(X)/N(H)$ is the abundance of the element relative to hydrogen; $N(H)/N_\mathrm{e}$ is the hydrogen density relative to the density of free electrons (≈0.83).

For plasma density diagnostics, the contribution function is used

$$C\left(T,\lambda_{ij},N_\mathrm{e}\right)= \\ =\frac{h_\mathrm{p}\nu_{ij}}{4\pi}\frac{A_{ji}}{N_\mathrm{e}}\frac{N_j\left(X^{+\mathrm{m}}\right)}{N\left(X^{+\mathrm{m}}\right)}\frac{N\left(X^{+\mathrm{m}}\right)}{N(X)}\left[\mathrm{erg\ cm^3 s^{-1}}\right], \quad (9)$$

related to the intensity by the following expression

$$I\left(\lambda_{ij}\right)=\int Ab(X)C\left(T,\lambda_{ij},N_\mathrm{e}\right)N_\mathrm{e}N_\mathrm{H}dh. \quad (10)$$

The level population j can be calculated by solving equations of statistical equilibrium comprising all important mechanisms of collisional and radiative excitation and deexcitation:

$$N_j\left(N_\mathrm{e}\sum_i C^\mathrm{e}_{ji}+N_\mathrm{p}\sum_i C^\mathrm{p}_{ji}+\sum_{i>j}R_{ji}+\sum_{i<j}A_{ji}\right)= \\ =\sum_i N_i\left(N_\mathrm{e}C^\mathrm{e}_{ij}+N_\mathrm{p}C^\mathrm{p}_{ij}\right)+\sum_{i>j}N_iA_{ij}+\sum_{i<j}N_iR_{ij}, \quad (11)$$

where C^e_{ji} and C^p_{ji} are the coefficients of the rate of excitation by electron and proton collisions ($\mathrm{cm^{-3}s^{-1}}$), R_{ji} are the coefficients of the rate of stimulated absorption ($\mathrm{s^{-1}}$).

2. RESULTS OF COMPARISON BETWEEN CALCULATED AND OBSERVED VALUES

2.1. Coronal emission line intensity

The evaluation of the quiet corona model in the form proposed by Krissinel [2015] has shown that it needs a little refinement in the UV range. This was due primarily to the need to reconcile calculated and experimental parameters of emission lines emitting in different temperature ranges.

The temperature distribution along the length of loop in formula (1) is determined by a_lp. Given small a_lp, the predominant part of loop length has a temperature close to the temperature of apices. In this case, the calculated intensity of emission lines of high-temperature ions increases, whereas the intensity of lines in the transition region decreases. This leads to a compromise: a_lp is considered equal to 0.31 at the loop apex and 0.6 at heights where the temperature is below the maximum one by 50 %.

The second refinement was dictated by the need to reduce the irregularity of the intensity profile above the limb. Accordingly, the number of loops has been increased to 12. After correction, the base pressures of loops p_0 (at h_0) increase monotonically with decreasing loop size from $2.1\cdot10^{-8}$ to $3.2\cdot10^{-8}$ dyn $\mathrm{cm^{-2}}$; and the pressures at apices, from 0.67 to 0.89 relative to p_0. At the same time, electron densities at loop apices increase with decreasing R_loop from $3.6\cdot10^8$ to $8.7\cdot10^8$ $\mathrm{cm^{-3}}$.

The adjustment of parameters has little effect on the results of calculations of the intensity of the model of the quiescent solar corona. Figure 1, which shows calculated and experimental brightnesses at the center of the solar disk at wavelengths from 1 to 31.6 cm, demonstrates good agreement between theoretical and experimental data.

The emission line intensity is calculated using the CHIANTI database; level populations are found by solving the set of equations with (11). The calculations show that the closest agreement with observations is reached through the fractional ionization from [Bryans et al., 2009].

Special attention is given to the choice of abundance *Ab*. As a result of the study it was assumed that coronal abundance values should be used as in [Feldman et al., 1992] for all elements except Si and Fe. For these elements, the abundance as compared to that in [Feldman et al., 1992] is reduced by 70 %, which correlates well with the data obtained in [Fludra, Schmelz, 1999; Schmelz et al., 2012].

Experimental data on UV plasma emission intensity over quiescent solar regions, obtained in different years and with different instruments, have a considerable, up to three times, spread in magnitude, which is caused by instrument calibration errors and differences in signal processing techniques. In this regard, this paper compares the data with SUMER, EIS, and CDS data [Warren, 2005; Brooks, Warren, 2006; Brooks et al., 2009; Warren, Brooks, 2009] acquired using the same signal processing technique.

Table 1 lists calculated (by (4)) I_th and observed I_obs intensities of 162 emission lines at the center of the solar disk and above the limb (at a distance of 1.07 optical radius of the quiet Sun).

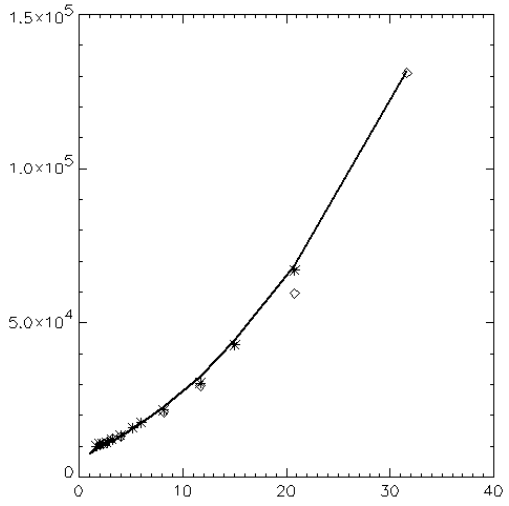

Figure 1. Calculated and experimental brightness values at centimeter and decimeter wavelengths. Along the X-axis is the wavelength (cm), along the Y-axis is the brightness temperature (K). Observable values from [Zirin et al., 1991] are marked with asterisk; from [Borovik et al., 1992], with diamond

For the analysis, I have selected emission lines with formation temperature above log(*T*)=4.9, corresponding to the emission from the corona and upper part of the transition region. The 10th and 11th columns show ratios of calculated values to observed ones (for measurements made with several telescopes, a mean value is taken).

The accuracy of measuring the intensity is determined by the accuracy of calibrating a spectrograph and by the error in identifying emission lines, which depends on a number of circumstances. For example, Brooks and Warren [2006] have noted that in some lines the spread of intensity when two independent processing techniques are employed significantly exceeds normal 20 %. The accuracy of calibrating instruments is also about 20 %, therefore the total error in intensity measurements cannot be less than 30 %. The far right column of Table 1 shows emission lines with identified blends; the blends decrease the accuracy of determining the intensity.

Let us first consider the calculated and observed values for the center of the solar disk. Observations are available for 136 lines. Figure 2, *a* is a histogram of ratios between calculated and experimental values. From the total number of lines the emission lines are excluded for which the calculated level is more than twice lower than the observed one and the blend (Mg VII 365.1 Å, Mg VIII 335.23 Å, and Fe XI 349.04 Å) is identified, as well as the O V 758.67, 759.44, 760.23, 760.44, and 762.00 Å lines whose low calculated level in [Doschek at el., 1999] is attributed to the inaccuracy of atomic data. The main part of the discrepancies is within 0.5–1.5. This indicates good agreement between the results.

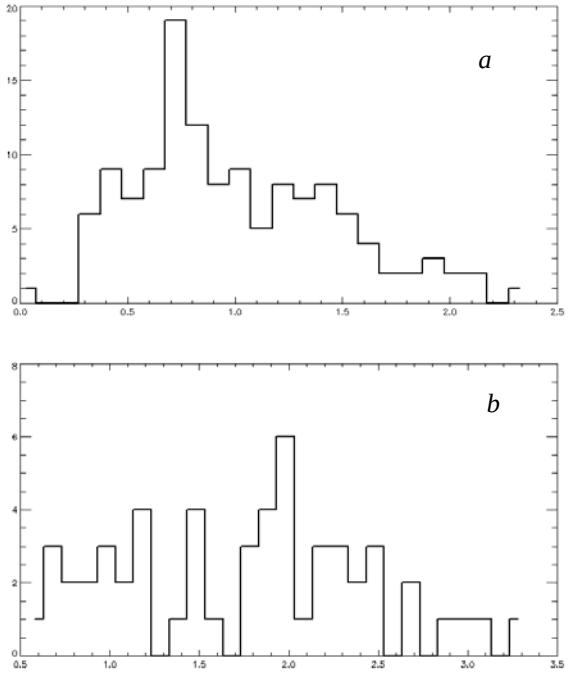

Figure 2. Histograms of ratios between calculated emission line intensities and experimental ones for the center of the solar disk (*a*) and above the limb (*b*)

Table 1

Calculated I_{th} and observed I_{obs} emission line intensities

λ, Å	I_{th}		I_{obs}					I_{th}/I_{obs}		Com.
	k_R		k_R					k_R		
	0.0	1.07	0.0				1.07	0.0	1.07	
			Br06	Br09	W05	W05	W09			
			CDS	EIS	CDS	SUM	EIS			
1	2	3	4	5	6	7	8	9	10	11
Ion Si VII										
275.3	17.84	8.960		10.52			11.54	1.69	0.77	
275.6	3.17	1.59					1.81		0.88	
278.4	5.69	2.86					2.95		0.97	
Ion Si VIII										
314.3	17.51	39.85	22.39		27.32			0.71		
316.2	34.88	79.32	41.81		45.92			0.79		
319.8	52.07	118.2	49.92		69.20			0.87		
944.4	3.107	6.13			2.43			1.28		
Ion Si IX										
258.0	2.94	9.23					5.08		1.82	
341.9	11.69	40.01	16.11		20.3			0.64		
345.1	24.37	81.94	45.7		48.1			0.51		
349.8	30.39	100.2	38.2		43.3			0.74		bl(6)
676.5	0.385	1.25			0.71			0.54		
694.6	0.946	3.07			1.74			0.54		

Ion Si X										
253.7	10.33	38.1					12.84		2.97	
258.3	52.43	193.3		31.84			71.3	1.65	2.71	
261.0	22.60	84.12		16.61			43.34	1.36	1.94	
271.9	19.15	71.25		15.57			37.62	1.23	1.89	
277.2	15.72	58.50		10.06			28.83	1.56	2.03	
347.4	40.17	149.8	46.84		44.68			0.88		
356.0	25.31	92.69	27.85		24.33			0.97		bl(6)
Ion Si XI										
303.3	90.92	344.4	112.1		124.6			0.76		
580.9	2.622	9.938	4.03		4.09			0.64		bl(4)
Ion Si XII										
502.6	4.516	17.08	4.73		4.98			0.93		
Ion Mg VII										
365.1	5.12	0.43	6.13		9.95			0.64		
367.6	19.41	1.50	14.53		20.96			1.09		
Ion Mg VIII										
313.7	24.52	28.12	23.81		30.10			0.91		
315.0	68.48	77.26	59.15		71.83			1.04		
317.0	17.31	19.85	15.61		20.54			0.98		
335.2	11.82	13.49	24.75					0.48		
338.9	15.77	17.99	10.44		14.91			1.24		
Ion Mg IX										
368.0	277.1	769.5	220.7		279.4			1.11		
706.0	11.54	30.68			7.26			1.59		
749.5	1.97	5.47			1.15			1.71		
Ion Mg X										
609.7	137.9	485.9	93.87		101.2	78.47		1.51		
624.9	68.40	240.9	34.08		36.91	30.47		2.02		
Ion Al IX										
680.2.	0.02	0.061				0.85		0.02		
Ion Al XI										
550.0	6.84	25.89			2.88			2.37		
Ion Ca X										
557.7	16.49	41.03	7.16		9.08			2.03		
574.0	8.14	20.22	6.18		6.57			1.28		
1	2	3	4	5	6	7	8	9	10	11
Ion O III										
525.7	17.07		17.56		17.75			0.97		
599.5	38.57		35.47		35.71			1.08		
702.3	9.086					9.26		0.98		
702.9	11.13					27.32		0.41		
703.8	34.16					43.46		0.78		
832.9	14.24					17.72		0.80		
833.7	34.35					51.02		0.67		
835.0	10.71					11.69		0.92		
835.2	63.97					78.59		0.81		
Ion O IV										
553.3	31.37		21.43		22.40			1.57		
554.0	60.93		37.32		40.12			1.48		
554.5	156.7		103.2		111.7			1.46		
555.2	31.54		22.54		24.50			1.34		
608.9	29.5		16.28		17.73			1.73		
779.8	1.758					2.54		0.69		
787.7	89.12					58.46		1.52		
790.2	163.7					108.2		1.51		
1399.7	5.106					6.05		0.84		
1401.1	27.8					36.14		0.77		

Ion O V										
629.7	647.2		308.1		338.4	415.7		1.82		
758.6	0.84					6.07		0.14		
759.4	0.644					4.73		0.14		
760.2	0.481					4.16		0.11		
760.4	2.498					18.77		0.13		
761.12	0.743					0.71		1.05		
762.0	0.795					6.25		0.13		
774.51	2.52					1.66		1.52		
1218.3	52.58					89.66		0.59		
Ion O VI										
183.93	2.356	2.647					2.81		0.94	
184.11	4.736	5.321					4.82		1.10	
1031.9	186.2	68.09				353.9		0.53		
1037.6	92.79	33.93				192.0		0.48		
Ion S IV										
744.90	1.185					1.48		0.80		
748.39	2.144					2.89		0.74		
750.22	5.571					6.89		0.81		
753.76	1.193					1.49		0.80		
1072.9	4.529					9.66		0.47		
1073.5	0.452					0.57		0.79		
Ion S V										
696.62	1.288					0.88		1.46		
786.46	32.72					32.06		1.02		
Ion S VI										
706.4	0.196					0.46		0.43		
712.6	0.348					0.90		0.39		
933.3	6.926					19.11		0.36		
944.5	3.465					9.43		0.37		
Ion S X										
264.2	13.17	49.02		14.26			34.77	0.92	1.41	
Ion Ne IV										
357.8	2.388		5.49					0.43		
541.1	2.84		2.43		2.39			1.14		
542.0	5.681		4.72		4.64			1.21		
543.8	8.498		7.35		8.34			1.08		
1	2	3	4	5	6	7	8	9	10	11
Ion Ne V										
358.4	4.521		4.35					1.04		
569.8	6.803		5.27		5.40			1.27		
572.3	12.29		8.21		8.81			1.44		
Ion Ne VI										
558.6	11.47		8.44		9.59			1.27		
562.7	20.49				15.60			1.31		
1005.	1.169					0.85		1.37		
Ion Ne VII										
559.9	0.798				0.99			0.81		
561.3	0.591					0.85		0.69		
561.7	2.937					3.07		0.96		
564.5	0.959					2.2		0.44		
895.1	4.058					4.51		0.90		
Ion Ne VIII										
770.4	53.49	75.93				73.11		0.73		
780.3	26.79	37.88				36.78		0.73		

Ion N IV										
765.1	88.35					80.7		1.09		
Ion N V										
1238.	27.07					81.53		0.33		
1242.	13.53					38.51		0.35		
Ion Ar VIII										
713.8	1.304	1.294				1.26		1.03		
Ion Na IX										
681.7	5.86	14.47				3.2		1.83		
Ion Fe VIII										
185.2	34.30	16.13		19.73			18.54	1.74	0.87	
186.5	21.53	10.35		14.77			14.6	1.46	0.71	
194.6	9.946	4.14					5.38		0.77	
Ion Fe IX										
171.0	570.2	1141.					921.2		1.24	
188.4	27.49	57.68		14.13			31.28	1.94	1.84	
189.9	16.50	33.97		8.24			15.36	2.00	2.21	
197.8	18.91	42.94		8.78			21.02	2.15	2.04	
Ion Fe X										
174.5	411.2	1348.					572.5		2.35	bl(6)
177.2	226.8	743.4		109.7			308.2	2.06	2.41	
184.5	88.28	287.3		57.21			142.1	1.54	2.02	
190.0	24.82	80.78		20.34			52.74	1.22	1.52	
193.7	5.46	17.72		4.72				1.16		
195.1	3.09	9.94		4.35				0.71		
207.4	7.51	24.19					24.09		1.00	
257.2	36.6	122.9		47.66			122.6	0.77	1.00	bl(6)
345.7	20.00	63.87		28.65			24.37	0.75		
365.5	8.36	26.69		12.3			17.59	0.56		
Ion Fe XI										
180.4	315.7	1164.		190.5			432.2	1.66	2.69	
182.1	48.41	176.5		21.95			58.50	2.20	3.02	
188.16	152.4	561.4		93.95			224.9	1.62	2.49	
188.21	89.96	331.6		64.03			153.1	1.40	2.17	
192.8	31.01	114.2					57.73		1.98	bl(7)
257.5	10.94	30.61					24.29		1.63	
257.7	6.38	23.12					11.72		1.97	
341.1	9.83	35.94	11.96		11.62			0.84		
349.0	2.55	9.14			9.51			0.27		bl(3)
352.6	37.81	138.5	30.16		30.51			1.25		
369.1	11.39	41.76	8.55		7.97			1.38		
1	2	3	4	5	6	7	8	9	10	11
Ion Fe XII										
186.8	23.83	89.01					35.17		2.53	bl(1)
192.3	51.69	195.7		36.96			79.48	1.4	2.46	bl(1)
193.5	108.5	410.8		79.57			177.5	1.36	2.31	
195.1	160.4	607.2		135.3			274.6	1.18	2.21	bl(1)
196.6	7.57	28.26					11.0		2.57	bl(7)
203.7	8.07	30.31					20.32		1.49	
256.4	6.03	22.78		13.62			39.09	0.44	0.58	
346.8	9.16	34.65	10.0		10.27			0.90		
352.1	17.71	67.01	21.0		19.52			0.87		
364.4	29.66	112.2	31.42		34.06			0.90		bl(1)
1242.	2.19	8.24				4.14		0.53		

Ion Fe XIII										
196.5	1.51	5.64					2.71		2.08	
197.4	2.94	11.17					7.10		1.57	
200.0	5.76	21.57					9.43		2.29	
201.1	14.28	54.22					45.14		1.20	bl(1)
202.0	46.27	177.3		82.05			157.6	0.56	1.12	
203.7	7.99	29.94					25.0		1.2	bl(6)
204.9	4.39	16.68					8.19		2.04	
246.2	8.32	31.54					9.36		3.37	
251.9	15.96	60.52					19.33		3.13	
320.8	4.03	15.12	8.65					0.47		
348.1	8.67	33.17	10.43		10.24			0.84		
Ion Fe XIV										
211.3	15.95	60.37					39.47		1.53	
264.7	6.69	25.25		9.43			20.72	0.71	1.22	
270.5	4.13	15.61					6.96		2.24	
274.2	9.035	34.20		11.26			18.31	0.80	1.87	
334.1	6.45	24.41	8.52		8.87			0.74		
Ion Fe XV										
284.1	11.46	43.23		13.16			21.20	0.87	2.04	

Note: units of intensity – erg cm^{-2} sr^{-1}.

Notation: k_R is the distance from the center of the solar disk in fractions of the solar radius; Br06 is the work by Brooks and Warren [2006]; Br09 is the work by Brooks et al. [2009]; W05 is the work by Warren [2005]; CDS is the Coronal Diagnostic Spectrometer, SOHO; EIT is the Extreme Ultraviolet Imaging Telescope, SOHO; SUM is SUMER (Solar Ultraviolet Measurements of Emitted Radiation, SOHO); EIS is the EUV Imaging Spectrometer, Hinode; bl(1) is the blend according to [Binello et al., 2001], bl(2) is the blend according to [Brown et al., 2008], bl (3) is the blend according to [Landi et al., 2002a; b], bl(4) is the blend according to [Brooks, Warren, 2006], bl(5) is the blend according to [Warren, 2005], bl(6) is the blend according to [Young et al., 1998], bl(7) is the blend according to [Young et al., 2007].

2.2. Equatorial distribution of emission intensity

Center-to-limb distributions in the UV range has been examined so far mainly when studying the effect of emission line broadening nearby and above the limb [Kjeldseth Moe, Nicolas, 1977; Mariska et al., 1978, 1979; Hassler et al., 1990; Erdely et al., 1998; Peter, 1999; Wilhelm et al., 1998; Lee et al., 2000]. These studies were generally not aimed at determining parameters of distribution over quiescent solar regions – magnitude of the peak above the limb, its position and width, and slope of the intensity decay above the limb. Parameters (angular and temporal resolutions, exposure time, and pointing accuracy) in these observations were inconsistent with the problem as posed.

Table 2 lists calculated ratios of the intensity maximum for a number of transition region lines on the limb to the intensity at the solar disk center χ, the position of the maximum intensity relative to the optical limb X (arcsec), and the angular distance R_{01} (arcsec) at which the intensity becomes lower than 0.01 (the C III and C IV lines were calculated regardless of the intensity decay). Some numerical values derived by Wilhelm et al. [1998] are also given for reference.

The equatorial distribution of emission lines was computed with a step of 0.25″ on the limb, and then smoothed on an interval of 2″ to approach technical constraints of real observations. Table 2 suggests that χ rises as the emitting region approaches the chromosphere. This is not seen in the data acquired by Wilhelm et al., [1998], which indicates technical difficulties in measuring limb parameters in transition region lines, where the width of the intensity peak is several angular seconds.

Table 2

Parameters of intensity distribution of transition region lines near the limb

Ion	Wavelength, Å	T_{max}, K	Calculation			Wilhelm-1998	
			χ	X	R_{01}	χ	X
C III	977.02	79432.8	26.33	+2.37	+4.57	3.25	+1.8
C IV	1548.19	100000.	22.23	+2.37	+4.77	10.5:12.8	+2.8
O IV	787.71	158489.	10.21	+2.37	+4.57	3.7:3.99	+2.5
S V	786.47	158489.	9.42	+2.37	+4.57	3.38	+2.5
S VI	944.52	199526.	6.28	+2.37	+24.17	10.2	+2.6
O V	629.73	251189.	6.28	+2.17	+5.17	4.59:4.95	+2.5
Ne VIII	770.41	630958.	5.09	+2.5	+300		

Notation: T_{max} is the temperature of the maximum ionization of the element ion; χ is the ratio of the intensity of the peak on the limb to the intensity at the disk center; χ is the position of the peak relative to the optical limb (arcsec); R_{01} is the distance from the optical limb at which the intensity becomes lower than 0.01 of the emission intensity above the disk center (arcsec); Wilhelm-1998 are the measurements of center/limb parameters according to [Wilhelm et al., 1998].

As the temperature of ionization maximum increases, the brightening on the limb expands, and the intensity decay above the limb becomes slower. Figure 3, *a* demonstrates this through equatorial distributions of Fe emission intensities. Notice that the lower is the ionization temperature in the emission line, the higher is the peak on the limb and the rate of intensity increase before the limb. This is because with decreasing temperature of line formation, the height of the emitting region decreases and its size increases along the line of sight on the limb versus the size at the disk center.

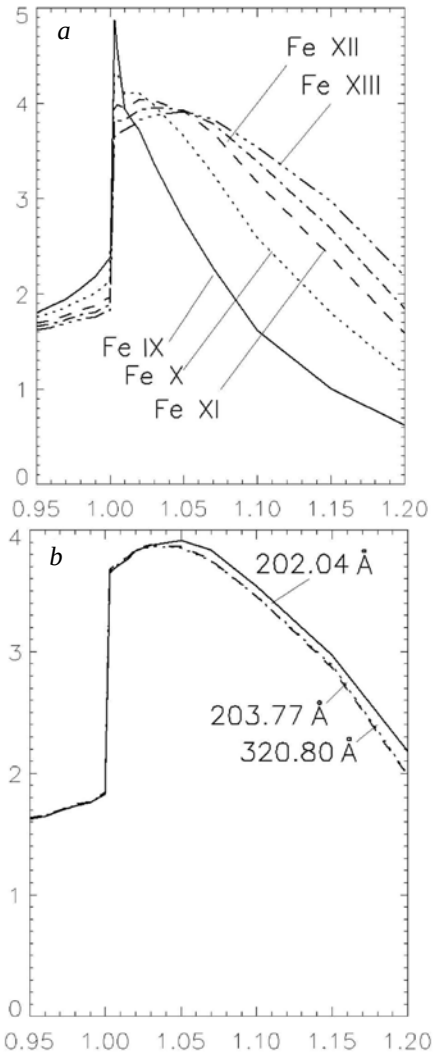

Figure 3. Normalized equatorial distributions of emission line intensity (*a*): Fe IX 197.8 Å, Fe X 190.0 Å, Fe XI 180.40 Å, Fe XII 193.50 Å, Fe XIII 202.04 Å. Along the X-axis is the distance from the center of the solar disk in fractions of the solar radius. Along the Y-axis is the normalized emission intensity at the solar disk center. Normalized Fe XIII intensity at the solar disk center as a function of height above the limb (*b*); along the X-axis is the distance from the solar disk center in fractions of the solar radius

The rate of intensity decay in lines of the same ion depends on the degree of density sensitivity: the larger is the sensitivity, the greater is the contribution to the total emission from middle and lower parts of loops and small loops being denser than large ones. Therefore, with distance from the limb when these emitting elements are out of the line of sight, the total intensity decreases more significantly. Figure 3, *b* plots normalized intensities of several Fe XIII lines at the solar disk center as a function of distance above the limb. As we can see, the difference in the rate of intensity decay may be significant.

3. DISCUSSION

Theoretical data on emission line intensity have been assessed using CDS, SUMER, and EIS observations made by different groups of researchers. However, for technical reasons there are only few observations of the same emission line made with different instruments. Table 1 shows that CDS observations of emission from the solar disk center, obtained in [Warren, 2005; Brooks, Warren, 2006], basically coincide within ~10 %, but there are differences up to 60 %. SUMER observations are made at a long wavelength, and the rare cases of agreement with CDS data do not allow us to evaluate the relative accuracy of measurements.

Of particular interest are the measurements made with EIS whose frequency range does not overlap with frequencies of other instruments. Meanwhile, the most thorough study of the quiet Sun above the limb based on a large number of emission lines has been carried out with this instrument. The results of comparison between calculated and experimental data for the emission above the limb, given in Table 1, show a wide spread of ratios – from 0.6 to 3.3. The discrepancies can be caused by different reasons: inaccurate atomic data, fractional ionization, errors in determining the level population and height dependence of element abundance, calibration errors and its variations with time.

The discrepancies can be analyzed from the spread of intersections of curves of emission measure versus temperature plotted for lines of different ions. In the case of isothermal corona, formulas (9, 10) yield an expression for the *EM* emission measure:

$$EM(T) = \int n_e^2 dh = \frac{4\pi I_\lambda}{C(n_e, T)},$$

where I_λ is the emission line intensity. As is known [Allen et al., 2000], the $EM(T)$ curves calculated at fixed density for emission lines of different ions intersect at a point corresponding to plasma temperature. Let us make such calculations for the data above the limb, taking, by analogy with [Warren, Brooks, 2009], $\log(n_e)=8.3$.

Figure 4, *a* presents the $EM(T)$ dependences for theoretical data. From all the wavelength ranges listed in Table 1, emission lines are excluded here whose calculated emission measure changes by more than 10 % with density changing by a factor of 10. These lines are Si IX 258.08 Å; Si X 253.78, 258.37 Å; S X 264.23 Å; Fe IX 189.94 Å; Fe X 257.26 Å; Fe XI 182.16 Å; Fe XII 186.88, 196.64, 203.72 Å; Fe XII 196.52, 200.02, 202.04, 203.79 Å; Fe XV 284 Å. All these lines differ in their increased sensitivity to density. The observed intensity, used to determine the emission measure, is proportional to the emissivity integral along the line of sight and for most lines corresponds to the product of emission measure and contribution function at a fixed density. If the density changes considerably along the line of sight, the integral emissivity for some lines turns out to be different, such that with the same emission measure the contribution function requires another density value. This is illustrated in Figure 4, *c*, which depicts maximum rated emissivity of one of the model loops for several Fe XII lines as a function of height. The 186.88, 196.64 и 203.72 Å emission lines exhibit a more abrupt change of emissivity with height than the 192.3, 193.5, and 195.11 Å lines.

In Figure 4, *a*, the intersection of the $EM(T)$ curves corresponds to $\log(T)=6.11$ and $\log(EM)=27.1$. Fluctuations of the intersection position do not exceed 0.05 (7 %) and refer largely to estimated errors in calculating fractional ionization for the emission lines whose ionization peak

temperature is far removed from the intersection temperature (Si VII, Fe XIV).

Figure 4, *c* presents temperature and density distributions in the longest loop of the corona model over the height from 0.07 *R*. Obviously, these parameters vary with height within relatively narrow limits. For smaller loops, these variations are lower still. Thus, the corona along the line of sight can be considered almost isothermal at a height of 1.07*R* above the limb.

Figure 4, *b* shows the *EM*(*T*) dependences derived from observations of the same set of wavelengths above the limb as in Figure 4, *a*. The intersections of the curves are seen to cover a vast area. The central point of intersection refers to log*T*=6.07 and log(n_e)=27.0. These values agree with the results obtained by Warren and Brooks [2009], if it is remembered that they have used other fractional ionizations and abundances. The spread of intersection positions corresponds to the difference between calculated and observed intensities.

The *EM*(*T*) dependences have been studied in many works (for example, [Allen et al., 2000; Landi et al., 2002a, b; Landi, Feldman, 2003, Warren, Brooks, 2009]). In some papers, the wide spread of intersections is attributed to the non-isothermal nature of the corona at the height where measurements have been made. It should, however, be noted that if along the line of sight in the corona there are atmospheric regions differing sharply in temperature, all emission lines of the same ion have nearly identical deflection from the intersection. In fact, these deflections are completely different.

For ions with line intensities measured throughout the EIS wavelength range, the calculated and observed values above the limb vary greatly: from 1.2 to 2.2 for Fe IX; from 1.0 to 2.4 for Fe X; from 1.6 to 3.0 for Fe XI; from 0.6 to 2.5 for Fe XII; and from 1.12 to 3.3 for Fe XIII. This was discussed by Warren and Brooks [2009] who made an assumption about technical reason for this effect – the difference in calibration between detectors employed to measure long-wavelength and short- wavelength lines.

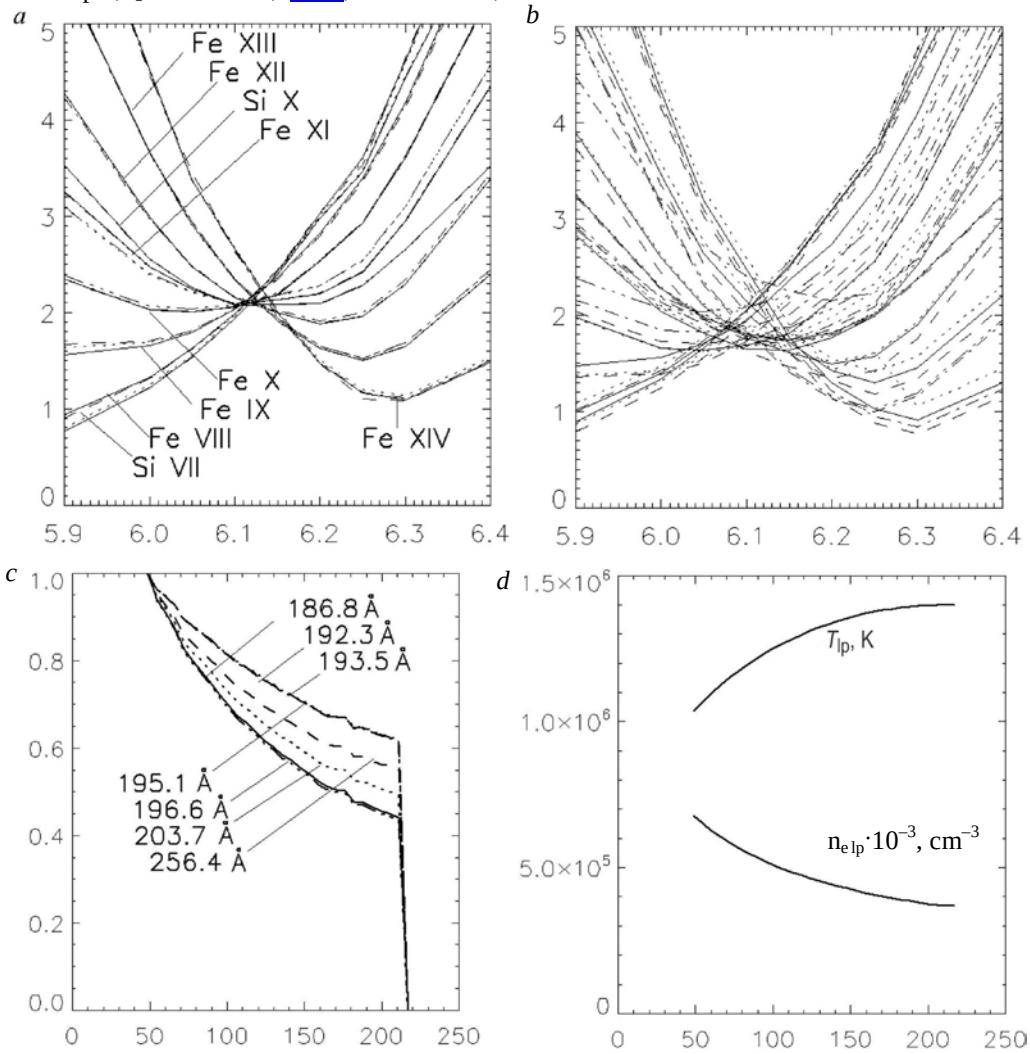

Figure 4. Analysis of the emission measure of Si and Fe lines in the corona model (*a*) and from EIS observations (*b*) (along the X-axis is log(*T*), along the Y-axis is log(*EM*) (cm^{-5})); emissivity of loop parts with R_{loop}=210 000 km for a number of Fe XII lines as a function of height (*c*); temperature and density distributions over the longest loop of the corona model at heights from 0.07 *R* (*d*). Along the X-axis is the distance from the photosphere, Mm

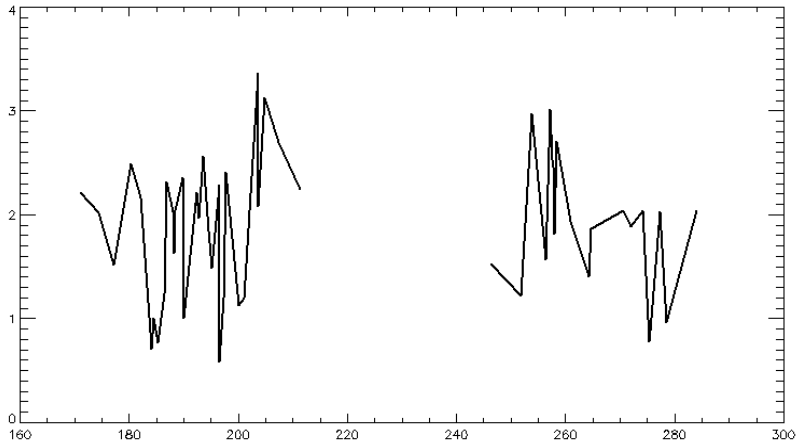

Figure 5. Spectrum of differences between calculated and experimental data above the limb. Along the X-axis is wavelengths (Å); along the Y-axis, the ratio between calculated and observed values

In Figure 5 that presents ratios between calculated and observed data for the entire EIS wavelength range, this reason is not primary.

The analysis of data for the solar disk center shows that line intensities of one ion measured with CDS or SUMER generally exceed calculated values, whereas intensities measured with EIS are always lower than calculated ones.

All the above details of the differences between the experimental and calculated values suggest that the wide spread of differences above the limb and the considerable excess of errors over normal values result from inaccurate EIS measurements.

In [Warren, 2005; Brooks, Warren, 2006], the experimental values listed in Table 1 are checked against the calculated values obtained from the emission measure of a line group. For some lines, these estimates agree well with the differences given in Table 1 for the solar disk center. Thus, we can exclude cases where ratios between calculated and observed values exceed 2, if this has been established in [Warren, 2005; Brooks, Warren, 2006]. This is the case of the following lines: Al IX 680.39 Å, Ne IV 357.88 Å, O VI 1037.6 Å, N V 1238.3, 1242.8 Å, S VI 706.5, 712.68, 933.40, 944.55 Å. After these exclusions as well as those discussed in Section 3.2, there remain 119 of the total number of lines. Nevertheless, only in five lines the calculated values are from 0.5 to 0.38 of the observed ones, and in three lines the theoretical values are 2–2.2 times larger than the experimental values obtained with EIS.

In general, the results of calculation of the EUV and FUV emission line intensities with consideration of EIS measurement errors agree with the experimental data. Thus, the multicomponent model of the quiescent solar corona proposed in [Krissinel, 2015] is applicable to a wide wavelength range.

It should be noted here that there is a significant difference between radio and EUV emissions in terms of the contribution of free-matter emission. If in the short wavelength range (1–5 cm) the contribution of the free-matter emission is decisive (80–95 %), in the decimeter range it does not exceed 10 %. In the EUV range, this contribution does not exceed 16 % for transition region lines and 10 % for coronal lines; i.e. the primary EUV emission in quiescent solar regions is associated with the emission from loops. This means that motions of matter in quiescent coronal regions, which are driven by motions of free matter, can be studied (with respect to broadening and shift of the line profile) only for a high signal-to-noise ratio. At the same time, in coronal holes where the contribution of loop emission is much smaller, conditions for such studies appear to be more favorable.

In this paper, calculations of the emission line intensity allowed us to clarify temperature and density distributions over loops of the corona model, mainly in the transition region of loops. This is important for the theory of heat because these parameters characterize the heating rate.

On the other hand, the results of the study have shown a rather high level of measurement errors, especially for the EIS spectrograph. This complicates the diagnostics of solar plasma and the study of abundance [Feldman et al., 2009].

CONCLUSION

In this paper, calculated intensities at EUV and FUV wavelengths have been compared with experimental ones, using the multicomponent model of the quiescent solar corona proposed for studying emission at centimeter and decimeter wavelengths. The corona model has been slightly modified: the number of loops was increased and the height temperature and density profiles were corrected. The calculated values were compared with the CDS, SUMER, and EIS observations made by different groups of researchers.

The calculation was carried out using fractional ionization from [Bryans et al., 2009]. This provided satisfactory agreement between calculated and observed values, especially for the center of the solar disk. The analysis of discrepancies between data above the limb, where these discrepancies often exceed expected errors, has shown that they are most likely to be caused by EIS measurement errors.

The corona model makes it possible to estimate equatorial distributions of emission intensity. Because of the absence of center-to-limb observations with high spatial resolution, this paper demonstrates center-to-limb distributions of a number of coronal Fe lines and estimates distribution parameters for transition region lines. These estimates are consistent with those obtained in well-known experimental studies when technical constraints are taken into account.

Thus, the model of quiescent coronal regions is adequate to observe intensities both in optically thin emission lines and in the 1 cm – 1 m wavelength range. It appears that this model or the probabilistic approach to the corona emission used in the model can be employed to study the quiet Sun's atmosphere at all latitudes, coronal holes, and nonthermal motions in the corona. At the same time, this model is inadequate to describe chromospheric emission with insufficiently studied spatial characteristics of its components.

The results indicate difficulties in interpreting data from EUV telescopes. The problems of calibrating and controlling measurements can be solved to some extent by regular test observations of quiescent solar regions. The results can also be directly used to make appropriate adjustments.

I am grateful to the team of the Radio Astrophysical Department of ISTP SB RAS for fruitful discussion.

The work was financially supported by the Ministry of Education and Science of the Russian Federation.

The work is carried out as part of Goszadanie 2018, project No. 007-00163-18-00 of 12.01.2018.

REFERENCES

Allen R., Landi E., Landini M., Bromage G.E. An empirical test of different ionization balance calculations in an isothermal solar plasma. *Astron. Astrophys*. 2000, vol. 358, pp. 332–342.

Binello A.M., Landi E., Mason H.E., Storey P.J., Brosius J.W. A comparison between theoretical and solar Fe $_{XII}$ UV line intensity ratios. *Astron. Astrophys*. 2001, vol. 370, pp. 1071–1087. DOI: 10.1051/ 0004-6361:20010255.

Borovik V.N., Kurbanov M.Sh., Makarov V.V. Distribution on radio brightness of the quiet Sun in the 2–32 cm range. *Soviet Aston.* 1992, vol. 36, no. 9, pp. 656–663.

Brooks D.H., Warren H.P. The intercalibration of SOHO EIT, CDS-NIS, and TRACE. *Astrophys. J. Suppl. Ser*. 2006, vol. 164, no. 1, pp. 202–214.

Brooks D.H, Warren H.P, Williams D.R., Watanabe T. HINODE/extreme – ultraviolet imaging spectrometer observations of the temperature structure of the quiet corona. *Astrophys. J*. 2009, vol. 705, no. 1, pp. 1522–1532. DOI: 10.1088/ 0004-637X/705/2/1522.

Brown C.M., Feldman U., Seely J.F., Korendyke C.M., Hara H. Wavelengths and intensities of spectral lines in the 171–211 and 245–291 Å ranges from five solar regions recorded by Extreme-ultraviolet Imaging Spectrometer (EIS) on Hinode. *Astrophys. J. Suppl. Ser*. 2008. vol. 176. pp. 511–535.

Bryans P., Landi E., Savin D.W. A new approach analyzing solar spectra and updaten collisional ionization equilibrium calculations. II. Updaten ionization rate coefficients. *Astrophys. J*. 2009, vol. 691, no. 2, pp. 1540–1559. DOI: 10.1088/0004-637X/691/2/1540.

Dere K.P., Landi E., Mason H.E., et al. CHIANTI – an atomic database for emission lines. *Astron. Astrophys. Suppl. Ser*. 1997, vol. 125, pp. 149–173.

Doschek E.E., Laming G.A., Doschek G.A., Feldman V., Wilhelm K. A comparison of measurements of solar extreme-ultraviolet spectral line intensities emitted by C, N, O, and S ions with theoretical calculations. *Astrophys. J*. 1999. vol. 518, no. 2. pp. 909–917.

Erdely R., Doyle J.G., Perez M.E., Wilhelm K. Center-to-limb width measurements of solar chromospheric, transition region and coronal lines. *Astron. Astrophys*. 1998, vol. 337, pp. 287–293.

Feldman U. Elemental abundances in the upper solar atmosphere. *Physica Scripta*. 1992, vol. 46, pp. 202–220.

Feldman U., Mandelbaum P., Seely J.L., Doschek G.A., Gursky H. The potential for plasma diagnostics from stellar extreme-ultraviolet observations. *Astron. Astrophys. Suppl. Ser*. 1992, vol. 81, pp. 387–408.

Feldman U., Schühle U., Widing K.G., Laming J.M. Coronal composition above the solar equator and the north pole as determined from spectra acquired by the SUMER instrument on SOHO. *Astrophys. J*. 1998, vol. 505, no. 2, pp. 99–1006.

Feldman U., Doschek G.A., Schühle U., Wilhelm K. Properties of quiet-Sun coronal plasmas at distances of 1.03 $\leq R_o \leq$1.50 along the solar equatorial plane. *Astrophys. J*. 1999, vol. 518, no. 1, pp. 500–507.

Feldman U., Warren H.P., Brown C.M., Doschek G.A. Can then composition of the solar corona be derived from HINODE/extreme-ultraviolet imaging spectrometer spectra. *Astrophys. J*. 2009, vol. 695, no. 1, pp. 36–45. DOI: 10.1088/ 0004-637X/695/1/36.

Fludra A., Schmelz J.T. The absolute coronal abundance of silfur, calcium, and iron from YOHKOH-BCS flare spectra. *Astr. Astrophys*, 1999, vol. 348, pp. 286–294.

Fontenla I.M., Avrett E.H., Loeser R. Energy balance in the solar transition region. III. Helium emission in hydrostatic, constant- abundance models with diffusion. *Astrophys. J*. 1993, vol. 406, no. 1, pp. 319–345.

Getman K.V., Livshits M.A. A model for the outer solar atmosphere devoid of activity. *Astronomicheskii zhurnal* [Astron. Report]. 1996, vol. 73, pp. 119–124. (In Russian).

Hassler D.M., Rottman G.J., Shoub E.C., Holzer T.E. Line broadening of Mg X λλ609 and 625 coronal emission lines observed above the solar limb. *Astrophys. J*. 1990, vol. 348, no. 1, pp. L77–L80.

Kjeldseth Moe O., Nicolas K.R. Emission measures, electron densities, and nonthermal velocities from optically thin UV lines near a quiet solar limb. *Astrophys. J*. 1977, vol. 211, pp. 579–586.

Krissinel B.B. Modeling of the structure of quiescent areas of the solar atmosphere emitting at 1–100 cm. *Astron. Rep*. 2015, vol. 59, no. 1, pp. 58–71. DOI: 10.1134/ S1063772915010060.

Laming J.M., Feldman U., Schühle U., Lemaire P., Curdt W., Wilhelm K. Electron density diagnostic for solar upper atmosphere from spectra obtained by SUMER/SOHO. *Astrophys. J*. 1997, vol. 485, pp. 911–919.

Landi E., Feldman U., Dere K.P. CHIANTI – an atomic database for emission lines. V. Comparison with an isothermal spectrum with SUMER. *Astrophys. J. Suppl. Ser*. 2002a, vol. 139, no. 1, pp. 281–296.

Landi E., Feldman U., Dere K.P. A comparison between coronal emission lines from an isothermal spectrum obtained with the coronal diagnostic spectrometer and CHIANTI emissivities. *Astrophys. J*. 2002b, vol. 574, no. 2, pp. 495–503.

Landi E., Feldman U. Properties of solar plasmas near solar maximum above two quiet regions at distance of 1.02 – 1.34 Ro. *Astrophys. J*. 2003, vol. 592, no. 1, pp. 607–619.

Landi E., Del Zanna G., Young P.R., Dere K.P., Mason H.E. CHIANTI – an atomic database for emission lines. XII, Version 7

for database. *Astrophys. J.* 2012, vol. 744, no. 2, p. 99. DOI: 10.1088/0004-637X/778/1/29.

Lantos P., Kundu M.R. The quiet Sun brightness distributions at millimeter wavelenghts and chrospheric inhomogeneities. *Astron. Astrophys*. 1972, vol. 21, pp. 119–124.

Lee H., Yun H.S., Chae J. Nonthermal broadening of the UV lines observed at the limb of the quiet SUN. *J. Kor. Astron. Soc.* 2000, vol. 33, pp. 57–37.

Mariska J.T., Feldman U., Doschek G.A. Measurements of extreme-ultraviolet emission-line profilies near the solar limb. *Astrophys. J.* 1978, vol. 226, pp. 698–705.

Mariska J.T., Feldman U., Doschek G.A. Nonthermal broadening of the extreme ultraviolet emission lines near Solar limb. *Astron. Astrophys*. 1979, vol. 73, pp. 361–363.

Mason H.E., Monsignori Fossi B.C. Spectroscopic diagnostic in the VUW for solar and stellar plasmas. *Astron. Astrophys. Rev.* 1994, vol. 6, pp. 123–173.

Mohan A., Landi E., Dwivedeli B.N. On the extreme-ultraviolet/ultraviolet plasma diagnostics for nitrogen-like ions from spectra obtained by SOHO/SUMER. *Astrophys. J.* 2003, vol. 582, no. 1, pp. 1162–1171.

Parenti S., Landi E., Bromage B.J.I. SOHO-ULYSSES spring 2000 quadrature: coronal diagnostic spectrometer and SUMER results. *Astrophys. J.* 2003, vol. 590, no. 1, pp. 519–532.

Peter H. Analysis of transition-region emission-line profiles from full-disk scans of the Sun using the SUMER instrument on SOHO. *Astrophys. J.* 1999, vol. 516, no. 1, pp. 490–504.

Schmelz J.T., Reames D.V., von Steiger R., Basu S. Composition of the solar corona, solar wind, and solar energetic particles. *Astrophys. J.* 2012, vol. 755, no. 1, p. 33–40. DOI: 10.1088/0004-637X/755/1/33.

Warren H.P. Measuring the physical properties of the solar corona: results from SUMER/SOHO and TRACE. *Sol. Phys.* 1999, vol. 190, pp. 363–377.

Warren H.P., Warshall A.D. Temperature and density measurements in a quiet coronal streamer. *Astrophys. J.* 2002, vol. 571, no. 1, pp. 999–1007.

Warren H.P. A solar minimum irradiance spectrum for wavelengths below 1200Å. *Astrophys. J. Suppl. Ser.* 2005, vol. 157, no. 1, pp. 147–173.

Warren H.P., Brooks D.H. The temperature and density structure of the solar corona. I. Observations of the quiet Sun with the EUV imaging spectrometer on Hinode. *Astrophys. J.* 2009, vol. 700, no. 2, p. 762–773. DOI: 10.1088/0004-637X/700/1/762.

Wilhelm K., Lemaire P., Dammasch I.E., et al. Solar irradiances and radiances of UV and EUV lines during the minimum sunspot activity in 1996. *Astron. Astrophys*. 1998, vol. 334, p. 685–702.

Young P.R., Landi E., Thomas R.J. CHIANTI: an atomic database for emission lines. II. Comparison with the SERTS-89 active region spectrum. *Astron. Astrophys*. 1998, vol. 329, p. 291–314.

Young P.R., Del Zanna G., Mason H.E., Dere K.P., Landi E., Landini M., Doschek G.A., Brown Ch.M., Culhane J. Harra L.K., Watanabe T., Hara H. EUV emission lines and diagnostics observed with Hinode/EIS. *Publ. Astron. Soc. Japan*. 2007, vol. 59, p. S857–S864.

Zirin H., Baument B.M., Hurford G.J. The microwave brightness temperature spectrum of the quiet Sun. *Astrophys. J.* 1991, vol. 370, no. 1, p. 779–783.

How to cite this article

Krissinel B.B. Intensity of emission lines of the quiescent solar corona: comparison between calculated and observed values. *Solar-Terrestrial Physics.* 2018, vol. 4, no. 1, pp. 12–24. DOI: 10.12737/stp-41201802